Supplementary Information: Anisotropic vortex squeezing in synthetic Rashba superconductors: a manifestation of Lifshitz invariants

L. Fuchs, J. Schmidt, N. Hüttner, C. Baumgartner, S. Reinhardt, C. Strunk, and N. Paradiso*
Institut für Experimentelle und Angewandte Physik,
University of Regensburg, 93040 Regensburg, Germany

D. Kochan
Institut für Theoretische Physik, University of Regensburg, 93040 Regensburg, Germany and
Institute of Physics, Slovak Academy of Sciences, 84511 Bratislava, Slovakia

S. Gronin and G. C. Gardner
Birck Nanotechnology Center, Purdue University, West Lafayette, Indiana 47907 USA

T. Lindemann
Department of Physics and Astronomy, Purdue University, West Lafayette, Indiana 47907 USA and
Birck Nanotechnology Center, Purdue University, West Lafayette, Indiana 47907 USA

M. J. Manfra
Birck Nanotechnology Center, Purdue University, West Lafayette, Indiana 47907 USA
Department of Physics and Astronomy, Purdue University, West Lafayette, Indiana 47907 USA
School of Materials Engineering, Purdue University, West Lafayette, Indiana 47907 USA and
School of Electrical and Computer Engineering, Purdue University, West Lafayette, Indiana 47907 USA

GINZBURG-LANDAU EQUATIONS IN THE PRESENCE OF THE ISOTROPIC LIFSHITZ INVARIANT: GENERAL CONSIDERATIONS

On a phenomenological level, non-centrosymmetric polar superconductors governed by the Rashba spin-orbit coupling, and subjected to an external magnetic field $\mathbf{B} = \mathrm{rot}\,\mathbf{A}$, can be described by the Ginzburg-Landau (GL) functional for the free energy density [1]:

$$F[\psi, \mathbf{A}] = a(T)|\psi|^2 + \frac{b}{2}|\psi|^4 + \frac{1}{4m}(\mathbf{D}\psi)^* \cdot \mathbf{D}\psi + \frac{\mathbf{B}^2}{2\mu_0} + F_L[\psi, \mathbf{A}] \equiv F_{GL}[\psi, \mathbf{A}] + F_L[\psi, \mathbf{A}], \qquad (S.1)$$

where the pre-last term represents density of the magnetic energy and the last one the so called isotropic *Lifshitz invariant*. The latter stems from an interplay of the Rashba spin-orbit interaction, $H_R = \alpha_R(\mathbf{k} \times \mathbf{n}) \cdot \boldsymbol{\sigma}$, Zeeman coupling, $H_Z = g\mu_B \mathbf{B} \cdot \boldsymbol{\sigma}$ and the superconducting coherence, and its explicit form reads [1]:

$$F_L[\psi, \mathbf{A}] = -\frac{1}{2}\kappa(\mathbf{n} \times \mathbf{B}) \cdot \mathbf{Y}_\psi \equiv -\frac{1}{2}\kappa(\mathbf{n} \times \mathbf{B}) \cdot \left[(\psi)^*\mathbf{D}\psi + \psi(\mathbf{D}\psi)^*\right], \qquad (S.2)$$

wherein the Edelstein parameter κ,

$$\kappa = 3\frac{\alpha_R}{\hbar}\frac{g\,\mu_B}{v_F\,p_F}f_3\left(\frac{\alpha_R\,p_F}{\hbar\,\pi\,k_B T_c}\right) \simeq 3\frac{\alpha_R}{\hbar}\frac{g\,\mu_B}{v_F\,p_F} \quad \text{with} \quad f_3(x) \simeq 0.475\int\limits_0^\pi dt \sum_{n=0}^\infty \frac{\sin t\,(x\sin t)^2}{(2n+1)^3[(2n+1)^2 + (x\sin t)^2]}, \quad (S.3)$$

serves as a figure of merit of the non-centrosymmetry of polar systems. The meaning of different symbols/letters is set by the following notation, moreover, all quantities are assumed to be in SI units:

- ψ stands for the condensate (Cooper pair) macroscopic wave function in the GL approach, being in D spatial dimensions, the unit of ψ is $\mathrm{m}^{-D/2}$,

- $\mathbf{n}$ is the spin-orbit-coupling unit vector defining the polar axis, without a loss of generality we assume $\mathbf{n} = \hat{z} = (0, 0, 1)$, and α_R is the corresponding Rashba coupling,

- $\boldsymbol{\sigma}$ stands for the vector $\{\sigma_x, \sigma_y, \sigma_z\}$ of Pauli spin $\frac{1}{2}$-matrices, spin quantization axis is along $\mathbf{n}$,

- $\mathbf{A}$ is the vector potential and $\mathbf{B} = \mathrm{rot}\,\mathbf{A}$ is the total magnetic field (in-plane + out-of-plane w.r.t. the given polar axis $\mathbf{n}$). We employ the Coulomb gauge, i.e., $\mathrm{div}\,\mathbf{A} = 0$,

- $\mathbf{D} = \frac{\hbar}{i}\nabla - 2e\mathbf{A}$ is the covariant momentum operator,

- m, g and $e < 0$ are, correspondingly, the electron effective mass, effective g-factor and the electron charge,

- μ_0 and μ_B are, correspondingly, magnetic permeability and the Bohr magneton,

- $a(T) = \alpha_0(T - T_c)/T_c \leq 0$ and b are the conventional GL parameters, T_c is the critical temperature, and k_{B} the Boltzmann constant,

- p_F and v_F stand for the Fermi momentum and Fermi velocity,

- κ is the Edelstein coefficient of non-centrosymmetry (not to be confused with the Ginzburg-Landau parameter $\kappa_{GL} \equiv \lambda/\xi$), in SI units κ is expressed in m·C/kg.

Considering $F[\psi, \mathbf{A}]$ as a functional of ψ and $\mathbf{A}$, one derives in a standard way the first and second GL equations in the presence of non-centrosymmetry, along with a boundary condition on the interface between the superconductor and a vacuum (an insulator or normal metal):

$$\text{1st GL-Eq: } 0 = \frac{\delta F}{\delta \psi^*} \qquad 0 = \frac{1}{4m}\left[\mathbf{D} - 2m\kappa(\mathbf{n} \times \mathbf{B})\right]^2 \psi + \left[a(T) - m\kappa^2(\mathbf{n} \times \mathbf{B})^2\right]\psi + b|\psi|^2\psi, \qquad \text{(S.4)}$$

$$\text{2nd GL-Eq: } 0 = \frac{\delta F}{\delta \mathbf{A}} \qquad 0 = \mathrm{rot}\left[\frac{1}{\mu_0}\mathbf{B} + \frac{1}{2}\kappa\left(\mathbf{n} \times \mathbf{Y}_\psi\right)\right] - \frac{e}{2m}\mathbf{Y}_\psi + 2\kappa e|\psi|^2(\mathbf{n} \times \mathbf{B}), \qquad \text{(S.5)}$$

$$\text{boundary condition: } \qquad 0 = \hat{\boldsymbol{\nu}}_{\mathrm{out}} \cdot \left[\mathbf{D} - 2m\kappa(\mathbf{n} \times \mathbf{B})\right]\psi\Big|_{\mathrm{interface}}, \qquad \text{(S.6)}$$

where $\hat{\boldsymbol{\nu}}_{\mathrm{out}}$ (in general not necessarily related with $\mathbf{n}$) is the outer normal vector pointing from the superconductor to the vacuum (an insulator or normal metal). For a completeness, the 2nd GL equation can be written in the form of a Maxwell equation—namely the Ampere law:

$$\mathrm{rot}\,\boldsymbol{\mathcal{H}} = \mathbf{j}_s\,, \qquad \text{where} \qquad \text{magnetic field intensity: } \quad \boldsymbol{\mathcal{H}} = \frac{1}{\mu_0}\mathbf{B} - \boldsymbol{\mathcal{M}}, \qquad \text{(S.7)}$$

$$\text{magnetization: } \quad \boldsymbol{\mathcal{M}} = -\frac{1}{2}\kappa\left(\mathbf{n} \times \mathbf{Y}_\psi\right), \qquad \text{(S.8)}$$

$$\text{supercurrent: } \quad \mathbf{j}_s = \frac{e}{2m}\mathbf{Y}_\psi - 2\kappa e|\psi|^2(\mathbf{n} \times \mathbf{B}). \qquad \text{(S.9)}$$

1ST GL EQUATION FOR A THIN SUPERCONDUCTING FILM IN IN-PLANE AND OUT-OF-PLANE MAGNETIC FIELD

In what follows we assume that:

- the superconducting film is quasi-2D, lies in xy-plane, and is terminated on both sides by a vacuum i.e. $\pm\hat{\boldsymbol{\nu}}_{\mathrm{out}} \parallel \mathbf{n} = \hat{z} = (0,0,1)$,

- the film has an *extrapolation length* d and extends in the transverse direction within the interval $z \in [-\frac{d}{2}, +\frac{d}{2}]$; the extrapolation length $d = d_{\mathrm{geo}} + \mathcal{O}(1)\xi$, where d_{geo} is the true geometrical (i.e., physical) thickness of the Al film and ξ is the GL coherence length,

- the film is without pronounced in-plane crystallographic anisotropies, i.e., we assume in-plane C_{4v} (or higher C) symmetry—this is imprinted in the form of H_R,

- the vortex-generating (out-of-plane) component of magnetic field, $\mathbf{B}_z = B_z\hat{z} = (0,0,B_z)$, is perpendicular to the film,

- the in-plane component of magnetic field $\mathbf{B}_{ip}$ is pointing along the y-axis, i.e. $\mathbf{B}_{ip} = B_y\hat{y} = (0, B_y, 0)$,

then

- then the total magnetic field vector $\mathbf{B} = \mathbf{B}_z + \mathbf{B}_{ip} = (0, B_y, B_z)$, and the corresponding vector potential in the Coulomb gauge $\mathbf{A} = (-B_z\frac{y}{2}, B_z\frac{x}{2}, -B_y x)$,

- $\mathbf{n} \times \mathbf{B} = -B_y \hat{x} = (-B_y, 0, 0) \Rightarrow m\kappa^2 (\mathbf{n} \times \mathbf{B})^2 = m\kappa^2 B_y^2.$

As a comment, B_z and B_y are local magnetic fields near the vortex core and in principle they differ from the corresponding laboratory values. However, we expect the difference to be small owing to the fact that the film thickness is much smaller than both ξ and λ. Thus, the in-plane field is not expected to be significantly affected by the negligible in-plane screening currents. However, in this respect, it is difficult to model the role of the 2DEG, which is relatively thicker compared to the Al film. Also the out-of-plane component is expected to be similar to the applied B_z field, since the Pearl length $2\lambda^2/d$ is of the order of many micrometers.

We will solve the 1st GL equation near the vortex core region, for which we assume that B_y and B_z are not varying in space on the length scale of the coherence length ξ, and therefore we treat them as constants. Let us elaborate in detail on the 1st GL equation, Eq. (S.4):

$$0 = \frac{1}{4m}\left[\mathbf{D} - 2m\kappa(\mathbf{n} \times \mathbf{B})\right]^2 \psi + \left[a(T) - m\kappa^2(\mathbf{n} \times \mathbf{B})^2\right]\psi + b|\psi|^2\psi. \tag{S.10}$$

We consider each term individually.

- $[\mathbf{D} - 2m\kappa(\mathbf{n} \times \mathbf{B})] = \frac{\hbar}{i}\boldsymbol{\nabla} + (eB_z y + 2m\kappa B_y, -eB_z x, 2eB_y x),$

- $[\mathbf{D} - 2m\kappa(\mathbf{n} \times \mathbf{B})]^2 = -\hbar^2\Delta + 2\frac{\hbar}{i}(eB_z y + 2m\kappa B_y, -eB_z x, 2eB_y x)\cdot\boldsymbol{\nabla} + [(eB_z y + 2m\kappa B_y)^2 + e^2(B_z^2 + 4B_y^2)x^2],$

- shifting the y-coordinate $y = y_{new} - 2\kappa m B_y/(eB_z) \Rightarrow$

$$[\mathbf{D} - 2m\kappa(\mathbf{n} \times \mathbf{B})] = \frac{\hbar}{i}\boldsymbol{\nabla} + (eB_z y_{new}, -eB_z x, 2eB_y x) \tag{S.11}$$
$$= [\text{renaming: } y_{new} \mapsto y]$$
$$= \frac{\hbar}{i}\boldsymbol{\nabla} + (eB_z y, -eB_z x, 2eB_y x) \tag{S.12}$$

$$[\mathbf{D} - 2m\kappa(\mathbf{n} \times \mathbf{B})]^2 = -\hbar^2\Delta + 2\frac{\hbar}{i}(eB_z y_{new}, -eB_z x, 2eB_y x)\cdot\boldsymbol{\nabla} + [e^2 B_z^2 y_{new}^2 + e^2(B_z^2 + 4B_y^2)x^2] \tag{S.13}$$
$$= [\text{renaming: } y_{new} \mapsto y]$$
$$= -\hbar^2\Delta + 2\frac{\hbar}{i}(eB_z y, -eB_z x, 2eB_y x)\cdot\boldsymbol{\nabla} + [e^2 B_z^2 y^2 + e^2(B_z^2 + 4B_y^2)x^2] \tag{S.14}$$
$$= -\hbar^2\Delta - 2eB_z \hat{L}_z + 4eB_y\left(x\frac{\hbar}{i}\partial_z\right) + [e^2 B_z^2 y^2 + e^2(B_z^2 + 4B_y^2)x^2] \tag{S.15}$$

- $\left[a(T) - m\kappa^2(\mathbf{n} \times \mathbf{B})^2\right] = a(T) - m\kappa^2 B_y^2 = -|a(T)| - m\kappa^2 B_y^2 \leq 0.$

The shift of the y coordinate is mathematically immaterial, since it can be absorbed into a change of the origin of y-axis and in a redefinition of the order parameter wave function:

$$\psi(x, y, z) = \psi(x, y_{new} - \tfrac{2\kappa m B_y}{eB_z}, z) \equiv \tilde{\psi}(x, y_{new}, z).$$

For simplicity of notation and minimal proliferation of symbols, we denote y_{new} by y and $\tilde{\psi}(x, y, z)$ by $\psi(x, y, z)$. On the physical ground $\Delta y = \frac{2\kappa m B_y}{eB_z}$ gives a displacement of the vortex core centre—defined as a minimum of $|\psi|$—from the position of a maximum of the out-of-plane magnetic field penetrating the vortex.

After shifting and renaming the equation (S.10) reads:

$$0 = -\frac{\hbar^2}{4m}\Delta\psi - \frac{2eB_z}{4m}\hat{L}_z\psi + \frac{4eB_y}{4m}\left(x\frac{\hbar}{i}\partial_z\right)\psi + \frac{e^2}{4m}[B_z^2 y^2 + (B_z^2 + 4B_y^2)x^2]\psi - [|a(T)| + m\kappa^2 B_y^2]\psi + b|\psi|^2\psi. \tag{S.16}$$

We look for a solution ψ that separates the in-plane dependence from the transverse one:

$$\psi(x, y, z) \equiv \Psi(x, y)\cdot\Phi(z), \tag{S.17}$$

where $\Psi(x, y)$ accounts for the in-plane and $\Phi(z)$ for the out-of-plane order parameter wave function, respectively. Assuming $\Phi(z)$ is a real-valued function (transverse domain is simply connected), then

$$0 = -\frac{\hbar^2}{4m}\Phi\cdot(\partial_{xx} + \partial_{yy})\Psi - \frac{\hbar^2}{4m}\Psi\cdot\partial_{zz}\Phi - \frac{2eB_z}{4m}\Phi\cdot\hat{L}_z\Psi + \frac{4eB_y}{4m}\Psi\cdot\left(x\frac{\hbar}{i}\partial_z\right)\Phi$$

$$+ \frac{e^2}{4m}[B_z^2 y^2 + (B_z^2 + 4B_y^2)x^2]\Psi\cdot\Phi - [|a(T)| + m\kappa^2 B_y^2]\Psi\cdot\Phi + b|\Psi|^2\Psi\cdot|\Phi|^2\Phi. \tag{S.18}$$

Now, we average the last equation along the transverse direction within the extrapolation length $d = d_{\text{geo}} + \mathcal{O}(1)\xi$:

$$0 = -\tfrac{\hbar^2}{4m}\langle\Phi\rangle \cdot (\partial_{xx} + \partial_{yy})\Psi - \tfrac{\hbar^2}{4m}\Psi \cdot \langle\partial_{zz}\Phi\rangle - \tfrac{2eB_z}{4m}\langle\Phi\rangle \cdot \hat{L}_z\Psi + \tfrac{4eB_y}{4m}\Psi \cdot \left\langle\left(x\tfrac{\hbar}{i}\partial_z\right)\Phi\right\rangle$$

$$+ \tfrac{e^2}{4m}[B_z^2 y^2 + (B_z^2 + 4B_y^2)x^2]\Psi \cdot \langle\Phi\rangle - [|a(T)| + m\kappa^2 B_y^2]\Psi \cdot \langle\Phi\rangle + b|\Psi|^2\Psi \cdot \langle|\Phi|^2\Phi\rangle, \tag{S.19}$$

where the meaning of the angular brackets (transverse averaging) is as follows:

$$\langle f = f(z)\rangle = \frac{1}{d}\int_{-\frac{d}{2}}^{+\frac{d}{2}} dz\ f(z). \tag{S.20}$$

Doing so, we obtain:

$$\langle\partial_{zz}\Phi\rangle = \tfrac{1}{d}\left[\partial_z\Phi\big|_{z=+\frac{d}{2}} - \partial_z\Phi\big|_{z=-\frac{d}{2}}\right] = 0, \tag{S.21}$$

$$\langle\partial_z\Phi\rangle = \tfrac{1}{d}\left[\Phi(z=+\tfrac{d}{2}) - \Phi(z=-\tfrac{d}{2})\right] = 0, \tag{S.22}$$

$$\langle\Phi\rangle = \text{real constant} \neq 0. \tag{S.23}$$

In the equations above, we set to zero $\langle\partial_{zz}\Phi\rangle$ and $\langle\partial_z\Phi\rangle$. This is due to the boundary conditions, Eq. (S.6), that should be satisfied at two interfaces located at $z = \pm\frac{d}{2}$ ($\boldsymbol{\nu}_{\text{out}} = \pm\hat{z}$), we treat both in conjunction:

$$0 = \boldsymbol{\nu}_{\text{out}} \cdot \left[\mathbf{D} - 2m\kappa(\mathbf{n}\times\mathbf{B})\right]\Psi(x,y)\cdot\Phi(z)\big|_{z=\pm\frac{d}{2}} = \left[\boldsymbol{\nu}_{\text{out}}\cdot\mathbf{D} - 2m\kappa\underbrace{\boldsymbol{\nu}_{\text{out}}\cdot(\mathbf{n}\times\mathbf{B})}_{=0}\right]\Psi(x,y)\cdot\Phi(z)\big|_{z=\pm\frac{d}{2}} \tag{S.24}$$

$$\Updownarrow$$

$$0 = \tfrac{\hbar}{i}\Psi(x,y)\cdot\partial_z\Phi(z)\big|_{z=\pm\frac{d}{2}} \pm 2eB_y x\,\Psi(x,y)\cdot\Phi(z=\pm\tfrac{d}{2}), \tag{S.25}$$

$$\Updownarrow \text{ assuming } \Psi(x,y) \neq 0$$

$$0 = \tfrac{\hbar}{i}\partial_z\Phi(z)\big|_{z=\pm\frac{d}{2}} \pm 2eB_y x\,\Phi(z=\pm\tfrac{d}{2}). \tag{S.26}$$

The above two equations should be satisfied, correspondingly, for any point with $z = \pm\frac{d}{2}$ and arbitrary x and y, therefore, in the case when $B_y \neq 0$, the easiest way is to require that the function $\Phi(z)$ has the following properties:

$$\partial_z\Phi(z)\big|_{z=\pm\frac{d}{2}} = 0 \quad\text{and}\quad \Phi(z=\pm\tfrac{d}{2}) = 0, \tag{S.27}$$

that hold on the scale of the extrapolation length $d = d_{\text{geo}} + \mathcal{O}(1)\xi$.

Dividing Eq. (S.19) by $\langle\Phi\rangle \neq 0$ and assuming $\langle B_{y/z}\rangle = B_{y/z}$ we get the effective 1st GL equation for a thin 2D film:

$$\boxed{0 = -\tfrac{\hbar^2}{4m}(\partial_{xx} + \partial_{yy})\Psi - \tfrac{2eB_z}{4m}\hat{L}_z\Psi + \tfrac{e^2}{4m}\left[B_z^2 y^2 + (B_z^2 + 4B_y^2)x^2\right]\Psi - \left[|a(T)| + m\kappa^2 B_y^2\right]\Psi + \underbrace{\left(b\tfrac{\langle\Phi^3\rangle}{\langle\Phi\rangle}\right)}_{b_{\text{eff}}}|\Psi|^2\Psi} \tag{S.28}$$

We point out that, *in principle*, B_z and B_y alone are sufficient to introduce a certain vortex anisotropy even for $\kappa = 0$, as it can be deduced from Eq. S.28. This corresponds to the known effect of vortex axis tilt for superconductors of finite thickness in the presence of Meissner currents, here introduced by the field B_y. The shear force exerted by the Meissner currents makes the vortex axis leaning towards the x-direction, instead of being parallel to the z-axis as in the $B_y = 0$ case. The intersection of a tilted cylinder with the xy-plane is an ellipse, which is a way to interpret the anisotropy in Eq. S.28. Such trivial anisotropy is not relevant for our situation since (i) the thickness in our case is so small (7 nm of Al minus 2 nm of typical oxide) compared to $\xi = 73$ nm, that the resulting weak screening currents can only produce a very minor tilt; (ii) even a major tilt could not explain the large squeeze along *both* axes, which is the main results of our work. As explained below, the observed effect requires a finite Lifshitz invariant, namely, a finite B_y and a finite κ. Experimentally, the necessity of the spin-orbit (i.e. of the Lifshitz invariant) for the observation of the effect is confirmed by our control measurements on the Al/GaAs heterostructure, cf. gray symbols in Fig. 2a of the main text.

Vortex solution & vortex-core curvatures

In the ensuing we solve approximately for the vortex the following generic equation of the Gross-Pitaevskii type:

$$0 = -\mathsf{A}(\partial_{xx} + \partial_{yy})\Psi + \tfrac{\mathsf{B}}{i}(x\partial_y - y\partial_x)\Psi + \left[\mathsf{C}_x\, x^2 + \mathsf{C}_y\, y^2\right]\Psi - \boldsymbol{\alpha}\Psi + \boldsymbol{\beta}\,|\Psi|^2\Psi \qquad (\text{S.29})$$

where the following coefficients link Eq. (S.28) with Eq. (S.29):

$$\mathsf{A} = \tfrac{\hbar^2}{4m}\,, \qquad\qquad \mathsf{C}_x = \tfrac{e^2 B_z^2}{4m}\left(1 + 4\tfrac{B_y^2}{B_z^2}\right), \qquad\qquad \boldsymbol{\alpha} = |a(T)| + m\kappa^2 B_y^2\,, \qquad (\text{S.30})$$

$$\mathsf{B} = -\tfrac{\hbar e B_z}{2m} = \tfrac{\hbar|e|B_z}{2m}\,, \qquad\qquad \mathsf{C}_y = \tfrac{e^2 B_z^2}{4m}\,, \qquad\qquad \boldsymbol{\beta} = b_{\text{eff}} = b\,\tfrac{\langle\Phi^3\rangle}{\langle\Phi\rangle}\,, \qquad (\text{S.31})$$

Because of a certain similarity of Eq. (S.29) with the harmonic oscillator problem (apart from the $\boldsymbol{\beta}$ term) we are interested in a vortex solution in the form:

$$\Psi(x,y) = K(x + i\,\delta\, y)\exp[\tfrac{p}{2}x^2 + qxy + \tfrac{r}{2}y^2] \simeq [\text{vortex core region}] \simeq K(x + i\,\delta\, y) + O(x^2, y^2)\,, \qquad (\text{S.32})$$

where the approximation on the right side is valid only close to the center of the vortex core. The term $(x + i\,\delta\, y)$ defines a vorticity of the solution Ψ; for $\delta > 0$ (< 0) it wraps counter-clock-wise (clock-wise). Moreover, the asymptotic form of our ansatz for Ψ has in the vortex core region the same functional dependence on x and y (including the third powers) as the original Abrikosov solution, see e.g. Tinkham [2].

To obtain an analytical expression for the vortex curvatures, we shall need some further approximations.
Approximation 1: We linearize in (S.29) the non-linear term proportional to $\boldsymbol{\beta}$:

$$|\Psi(x,y)|^2] \simeq [\text{vortex core region}] \simeq K^2 x^2 + K^2\delta^2 y^2 \propto k_x x^2 + k_y y^2\,, \qquad (\text{S.33})$$

where $k_x \propto K^2$ and $k_y \propto \delta^2 K^2$ are the vortex curvatures along $\hat{x}$ and $\hat{y}$, respectively. Since we are interested in the vortex core region $\sqrt{x^2 + y^2} < \xi \ll \lambda$, we consider only the lowest order terms in $|\Psi|^2$ in Eq. (S.29). Doing so we get linear partial differential equations with the modified quadratic-potential terms:

$$0 = -\mathsf{A}(\partial_{xx} + \partial_{yy})\Psi + \tfrac{\mathsf{B}}{i}(x\partial_y - y\partial_x)\Psi + \Big[\underbrace{(\mathsf{C}_x + \boldsymbol{\beta} K^2)}_{\mathsf{C}_1}\, x^2 + \underbrace{(\mathsf{C}_y + \boldsymbol{\beta} K^2\delta^2)}_{\mathsf{C}_2}\, y^2\Big]\Psi - \boldsymbol{\alpha}\Psi \qquad (\text{S.34})$$

Plugging the ansatz, Eq. (S.32), into the above equation, we get a system of non-linear algebraic equations for the unknown parameters K, δ, p, q, r (the first two, K and δ, enter also C_1 and C_2):

$$0 = \mathsf{C}_1 - \mathsf{A}\, p^2 - i\,\mathsf{B}\, q - \mathsf{A}\, q^2 \qquad (\text{S.35})$$

$$0 = \mathsf{C}_2 - \mathsf{A}\, r^2 + i\,\mathsf{B}\, q - \mathsf{A}\, q^2 \qquad (\text{S.36})$$

$$0 = \mathsf{B}\, p - \mathsf{B}\, r + 2i\,\mathsf{A}\, p\, q + 2i\,\mathsf{A}\, q\, r \qquad (\text{S.37})$$

$$0 = 3\,\mathsf{A}\, p + 2i\,\mathsf{A}\, q\,\delta + \mathsf{A}\, r - \mathsf{B}\,\delta + \boldsymbol{\alpha} \qquad (\text{S.38})$$

$$0 = 3\,\mathsf{A}\, r\,\delta - 2i\,\mathsf{A}\, q + \mathsf{A}\, p\,\delta - \mathsf{B} + \delta\,\boldsymbol{\alpha} \qquad (\text{S.39})$$

For convenience of analytical calculation, we change the roles of δ and K with C_1 and C_2, i.e., we are assuming as unknowns: $p, q, r, \mathsf{C}_1, \mathsf{C}_2$, and as parameters: $\mathsf{A}, \mathsf{B}, \boldsymbol{\alpha}, \delta$.

For a given sign of B, we have the freedom to choose the sign of δ—both enter as parameters in the above equations. However, the basic physics of the superconducting vortices tells us that for $B_z > 0$ (implying also $\mathsf{B} > 0$) the vortex should wrap counter-clock-wise. This means that in our ansatz, Eq. (S.32), we should have for a positive (negative) B_z also positive (negative) δ—this physical requirement implies that combinations like $\mathsf{B}\delta$ or B/δ are always positive quantities. Solving Eqs. (S.35)-(S.39), we obtain two sets of solutions—C_1^+ and C_2^+—and—C_1^- and C_2^-—both can be

compactly written as follows:

$$\mathsf{C}_1^\pm = \frac{\alpha^2}{128\mathsf{A}} \left[\frac{\mathsf{B}^2}{\alpha^2}\left(\frac{9}{\delta^2} - 22 + 81\delta^2\right) + 20 \pm \left(6 + \frac{3\mathsf{B}}{\alpha\delta} + \frac{27\mathsf{B}\delta}{\alpha}\right)\sqrt{\frac{\mathsf{B}^2}{\alpha^2}\left(\frac{9}{\delta^2} - 14 + 9\delta^2\right) + 4\frac{\mathsf{B}}{\alpha}\left(\frac{1}{\delta} + \delta\right) + 4} + 4\left(\frac{5}{\delta} + 9\delta\right)\frac{\mathsf{B}}{\alpha} \right]$$
$$\equiv \mathsf{C}_x + \beta K^2 \tag{S.40}$$

$$\mathsf{C}_2^\pm = \frac{\alpha^2}{128\mathsf{A}} \left[\frac{\mathsf{B}^2}{\alpha^2}\left(\frac{81}{\delta^2} - 22 + 9\delta^2\right) + 20 \pm \left(6 + \frac{27\mathsf{B}}{\alpha\delta} + \frac{3\mathsf{B}\delta}{\alpha}\right)\sqrt{\frac{\mathsf{B}^2}{\alpha^2}\left(\frac{9}{\delta^2} - 14 + 9\delta^2\right) + 4\frac{\mathsf{B}}{\alpha}\left(\frac{1}{\delta} + \delta\right) + 4} + 4\left(\frac{9}{\delta} + 5\delta\right)\frac{\mathsf{B}}{\alpha} \right]$$
$$\equiv \mathsf{C}_y + \beta K^2\delta^2 \tag{S.41}$$

the formulas for p, q, r are not given since we do not need them explicitly—we are looking just for the functional form of Ψ in the first order in x and y. We now need to solve Eqs. (S.40) and (S.41) for K and δ, which is pretty difficult owing to the complicated expressions in square brackets in the above equations. Moreover, it is necessary to choose which set of solutions—either "+": $\mathsf{C}_1^+, \mathsf{C}_2^+$, or "−": $\mathsf{C}_1^-, \mathsf{C}_2^-$—is physically more appropriate. This shall be done at the end, when fitting the experimental data.

Approximation 2: To proceed further we expand the lengthy expressions for $\mathsf{C}_1^\pm$, and $\mathsf{C}_2^\pm$ entering Eqs. (S.40) and (S.41) assuming:

$$2\pi\frac{|B_z|\xi^2}{\Phi_0} \approx \left|\frac{\mathsf{B}}{\alpha}\right| \ll 1\,, \qquad \frac{\mathsf{B}}{\alpha\delta} \ll 1\,, \qquad \text{and} \qquad \frac{\mathsf{B}\delta}{\alpha} \ll 1\,. \tag{S.42}$$

By keeping therein terms only up to linear order in $\frac{\mathsf{B}}{\alpha}$, $\frac{\mathsf{B}}{\alpha\delta}$ and $\frac{\mathsf{B}\delta}{\alpha}$, a straightforward calculation gives:

$$\mathsf{C}_1^\pm = \frac{\alpha^2}{4^{1+(0.5-(\pm)0.5)}\mathsf{A}}\left[1 + \left(\frac{1}{\delta} \pm 3\delta\right)\frac{\mathsf{B}}{\alpha}\right]\,, \tag{S.43}$$

$$\mathsf{C}_2^\pm = \frac{\alpha^2}{4^{1+(0.5-(\pm)0.5)}\mathsf{A}}\left[1 + \left(\delta \pm \frac{3}{\delta}\right)\frac{\mathsf{B}}{\alpha}\right]\,. \tag{S.44}$$

Recalling that $\mathsf{C}_1^\pm = \mathsf{C}_x + \beta K^2$ and $\mathsf{C}_2^\pm = \mathsf{C}_y + \beta K^2\delta^2$, see Eq. (S.34), the problem reduces for each of the two cases—labeled by "+" and "−" sign—to a solution of the algebraic system of two nonlinear equations for two unknowns K and δ:

$$\mathsf{C}_1^\pm = \frac{\alpha^2}{4^{1+(0.5-(\pm)0.5)}\mathsf{A}}\left[1 + \left(\frac{1}{\delta} \pm 3\delta\right)\frac{\mathsf{B}}{\alpha}\right] = \mathsf{C}_x + \beta K^2\,, \tag{S.45}$$

$$\mathsf{C}_2^\pm = \frac{\alpha^2}{4^{1+(0.5-(\pm)0.5)}\mathsf{A}}\left[1 + \left(\delta \pm \frac{3}{\delta}\right)\frac{\mathsf{B}}{\alpha}\right] = \mathsf{C}_y + \beta K^2\delta^2\,. \tag{S.46}$$

Having found K and δ the problem is solved, since they provide—apart from a less relevant global scale factor—the curvatures of the vortex core, i.e., $k_x \propto K^2$, and $k_y \propto K^2\delta^2$, see Eq. (S.33).

To effectively solve the above systems of equations, it is useful to make explicit the following physical quantities (expressed in terms of the GL parameters $|a(T)|$ and β)

Bulk Cooper-pair density (per unit volume):	$f_0^2 = \dfrac{|a(T)|}{b} = \dfrac{\langle\Phi^3\rangle}{\langle\Phi\rangle}\dfrac{|a(T)|}{\beta}\,,$	(S.47)
Bulk condensation energy density (per unit volume):	$e_c^* = \dfrac{|a(T)|^2}{b} = |a(T)|f_0^2 = b\,f_0^4\,,$	(S.48)
Effective thermodynamic critical field B_c^*:	$B_c^* = \sqrt{2\mu_0 e_c^*}\,,$	(S.49)
GL coherence length:	$\xi = \dfrac{\hbar}{\sqrt{4m|a(T)|}}\,,$	(S.50)
Penetration length:	$\lambda = \sqrt{\dfrac{m}{2\mu_0 e^2 f_0^2}}\,,$	(S.51)
Lifshitz-Edelstein length:	$\ell_\kappa = \dfrac{1}{2\kappa\mu_0|e|f_0^2}\,,$	(S.52)
Superconducting flux quantum:	$\Phi_0 = \dfrac{h}{2|e|} = 2\pi\dfrac{\hbar}{2|e|}\,,$	(S.53)

We also use the derived quantities: $m\kappa^2 = \frac{1}{2\mu_0 f_0^2} \frac{\lambda^2}{\ell_\kappa^2}$ and $\frac{m\kappa}{|e|} = \frac{\lambda^2}{\ell_\kappa} \Rightarrow$

$$\frac{\boldsymbol{\alpha}^2}{\mathsf{A}\boldsymbol{\beta}} = \frac{\left(|a(T)| + m\kappa^2 B_y^2\right)^2}{\frac{\hbar^2}{4m} \boldsymbol{\beta}} = \frac{|a(T)|\,|a(T)|}{\frac{\hbar^2}{4m} \boldsymbol{\beta}} \left(1 + \frac{m\kappa^2}{|a(T)|} B_y^2\right)^2 = \frac{\langle\Phi\rangle}{\langle\Phi^3\rangle} \frac{f_0^2}{\xi^2} \left(1 + \frac{\lambda^2}{\ell_\kappa^2} \frac{1}{e_c^*} \frac{B_y^2}{2\mu_0}\right)^2, \tag{S.54}$$

$$\frac{\mathsf{C}_y}{\boldsymbol{\beta}} = \frac{e^2 B_z^2}{4m\,\boldsymbol{\beta}} = \frac{\langle\Phi\rangle}{\langle\Phi^3\rangle} \frac{1}{4} \frac{f_0^2}{\lambda^2} \frac{1}{e_c^*} \frac{B_z^2}{2\mu_0}, \tag{S.55}$$

$$\frac{\mathsf{C}_x}{\boldsymbol{\beta}} = \frac{\langle\Phi\rangle}{\langle\Phi^3\rangle} \frac{1}{4} \frac{f_0^2}{\lambda^2} \frac{1}{e_c^*} \frac{B_z^2}{2\mu_0} \left(1 + 4\frac{B_y^2}{B_z^2}\right), \tag{S.56}$$

$$\frac{\boldsymbol{\alpha}}{\boldsymbol{\beta}} \frac{\mathsf{B}}{\mathsf{A}} = \frac{\langle\Phi\rangle}{\langle\Phi^3\rangle} f_0^2 \left(1 + \frac{\lambda^2}{\ell_\kappa^2} \frac{1}{e_c^*} \frac{B_y^2}{2\mu_0}\right) \frac{2\pi\,B_z}{\Phi_0}, \tag{S.57}$$

We now define a dimensionless Cooper pair wave function: $\psi(x,y) = \Psi(x,y)/(\sqrt{\frac{\langle\Phi\rangle}{\langle\Phi^3\rangle}} f_0)$ and expand $|\psi(x,y)|^2$ around the vortex core center

$$|\psi(x,y)|^2 \simeq \frac{K^2}{\frac{\langle\Phi\rangle}{\langle\Phi^3\rangle} f_0^2} x^2 + \frac{K^2\delta^2}{\frac{\langle\Phi\rangle}{\langle\Phi^3\rangle} f_0^2} y^2 \equiv \frac{1}{2} k_x x^2 + \frac{1}{2} k_y y^2. \tag{S.58}$$

We have now all the ingredients to compute the curvatures of $|\psi|^2$ near the vortex core. Equation (S.58) links k_x and k_y with K and δ, which in turns are the solutions of the algebraic equations (S.45) and (S.46). The result below is made explicit for the "+" case:

$$\frac{1}{\xi^2} \left(1 + \frac{\lambda^2}{\ell_\kappa^2} \frac{1}{e_c^*} \frac{B_y^2}{2\mu_0}\right)^2 + \left(\sqrt{\frac{k_x}{k_y}} + 3\sqrt{\frac{k_y}{k_x}}\right) \left(1 + \frac{\lambda^2}{\ell_\kappa^2} \frac{1}{e_c^*} \frac{B_y^2}{2\mu_0}\right) \frac{2\pi B_z}{\Phi_0} \equiv \frac{1}{\lambda^2} \frac{1}{e_c^*} \frac{B_z^2}{2\mu_0} \left(1 + 4\frac{B_y^2}{B_z^2}\right) + 2k_x, \tag{S.59}$$

$$\frac{1}{\xi^2} \left(1 + \frac{\lambda^2}{\ell_\kappa^2} \frac{1}{e_c^*} \frac{B_y^2}{2\mu_0}\right)^2 + \left(\sqrt{\frac{k_y}{k_x}} + 3\sqrt{\frac{k_x}{k_y}}\right) \left(1 + \frac{\lambda^2}{\ell_\kappa^2} \frac{1}{e_c^*} \frac{B_y^2}{2\mu_0}\right) \frac{2\pi B_z}{\Phi_0} \equiv \frac{1}{\lambda^2} \frac{1}{e_c^*} \frac{B_z^2}{2\mu_0} + 2k_y, \tag{S.60}$$

since this set of equations turns out to provide a reasonable fit of the experimental data for small in-plane magnetic fields. Due to the significant non-linearity of the problem, it is not, however, excluded that at a certain elevated value of the in-plane field the system can come into a transition point, from which the "−" case solutions would start to be realized by nature.

Impact of the crystal structure symmetry. It is important to stress that the above derivation assumes C_{4v} crystallographic symmetry, which is higher than the actual symmetry of InAs-based 2DEG that is possessing the crystal symmetry C_{2v}. In principle, for a C_{2v}-symmetric crystal one might introduce two *different* Lifshitz lengths $\ell_{\kappa 1}$ and $\ell_{\kappa 2}$ for two different main crystallographic axes—or the so called anisotropic Lifshitz invariant: $\frac{1}{2}\kappa_1 B_y(\Psi^* \mathbf{D}_x \Psi + c.c.) + \frac{1}{2}\kappa_2 B_x(\Psi^* \mathbf{D}_y \Psi + c.c.)$. It turns out, however, that the best fit of our data does not require anisotropic Lifshitz invariant in order to produce the striking curvature enhancement as observed in the experiment. In other words, an isotropic spin-orbit interaction stemming from an isotropic Fermi surface is sufficient to produce an anisotropic vortex squeezing. The vortex anisotropy is exclusively due to the interplay of spin-orbit-coupling with the in-plane magnetic field.

Fitting experimental data

Equations (S.59) and (S.60) are the final output of our model: they implicitly link the curvature along the x and y-axis (k_x and k_y, respectively) to the Lifshitz length ℓ_κ and to the effective thermodynamic critical field B_c^*. We have experimentally determined the following constants:

$$\xi = 73 \text{ nm}, \qquad \lambda = 227 \text{ nm}, \qquad B_z = 10 \text{ mT}, \qquad B_{c2} = 61 \text{ mT}. \tag{S.61}$$

In particular, B_{c2} is determined as the B_z value (at base temperature and zero bias) for which a resistance emerges such that the RLC circuit resonance is damped. This resistance is, for the present experimental conditions, of the order of 65 Ω [3], which is much less that of half the normal resistance $0.5R_n = 0.5 \cdot 3074R_{n,\square} = 14.17$ kΩ, where $R_{n,\square} = R_n/3074 = 9.22$ Ω is the normal sheet resistance. Therefore the B_{c2} value above is slightly less than the conventional value, which is such that $R(B_z = B_{c2}) = 0.5R_n$. The value of ξ immediately follows from that of B_{c2} since $B_{c2} = \Phi_0/(2\pi\xi^2)$. The value of λ is determined from the sheet kinetic inductance ($L_s/N_\square$) at zero field and base temperature, which equals 13 pH. The sheet kinetic inductance provides directly λ via $L_{s,\square} = \mu_0\lambda^2/d$.

We can numerically solve Eqs. (S.59) and (S.60) for k_x and k_y as functions of the in-plane field B_y, using the experimentally given values of ξ, λ, and B_z, see Eq. (S.61), as fixed parameters. The Lifshitz length ℓ_κ and the effective condensation energy e_c^*—or equivalently B_c^*, since $e_c^* = (B_c^*)^2/(2\mu_0)$—are taken as the fitting parameters. In order to fit the experimental data displayed in Fig. 2**a** in the main text, we must relate the vortex curvatures with vortex inductances using

$$L_{v,\perp} = \frac{L_0}{2\xi^2 k_y}, \qquad\qquad L_{v,\parallel} = \frac{L_0}{2\xi^2 k_x}, \qquad\qquad \text{(S.62)}$$

where $L_{v,\perp}$ ($L_{v,\parallel}$) is the vortex inductance measured for $\mathbf{B}_{ip} \perp \mathbf{I}$ ($\mathbf{B}_{ip} \parallel \mathbf{I}$). Apart of ℓ_κ and B_c^* we also fit the conversion parameter L_0 that serves as a global scaling factor, its theoretical value depends on the microscopic details of the pinning strength.

If we restrict the fitting range of the in-plane field to [-0.1 T, 0.1 T] we obtain the solid line curves in Fig. 2**a** in the main text. The corresponding fitting parameters are:

$$L_0 = 2.02\,\mu\text{H}, \qquad \ell_\kappa = 594\,\text{nm}, \qquad \text{and} \qquad B_c^* = 96.1\,\text{mT}. \qquad\qquad \text{(S.63)}$$

The value of B_c^* is substantially higher than our independent estimate of the thermodynamic critical field $B_c = 13$ mT. This is due to the fact that we have assumed local microscopic in-plane field to be identical to the applied magnetic field. For a few-nm-thick Al film this is in good approximation true (since the thickness is much smaller than both λ and ξ), however, it is difficult to model the effect of the thicker 2DEG, which also plays a role. The discrepancy between local microscopic field and the applied field B_y might be the reason for the difference between the estimated $B_c = 13$ mT and the value of $B_c^* = 96.1$ mT obtained from the fit.

We notice that the model nicely captures the prompt decrease of the vortex inductance with the in-plane magnetic field, and the magnitude of the vortex inductance anisotropy. The fit quantitatively reproduces the data up to fields of the order of 100 mT. Above that field range, it systematically overestimates the vortex squeezing effects. A possible explanation for this overestimate is the suppression of the order parameter in the proximitized 2DEG, which recent experiments showed to take place precisely in this magnetic field range [4]. At the moment this is just an hypothesis, further study is needed to elucidate the relative contribution of 2DEG and Al to the superfluid density, as well as the role of the unconventional pairing to the vortex inductance, as discussed in the main text.

INDUCTANCE PER VORTEX IN THE LINEAR REGIME OF $L_v(B_z)$

Figure 1**c** of the main text shows the dependence of the vortex inductance L_v on the out-of-plane field B_z. In particular, the inset makes it evident that for moderate fields (up to 20 mT) the behavior is linear, i.e., each vortex added into the system contributes with the same additional inductance. This is what one would expect if the interaction between vortices is negligible. This is the case if the separation between votices is much larger then ξ or, equivalently, if $B_z \ll B_{c2}$. Eventually, when B_z becomes a significant fraction of B_{c2} (in our case for $B_z = 20$ mT $\approx B_{c2}/3$) then neighboring cores start overlapping and each new vortex also contributes to the reduction of the superfluid density in its vicinity, producing a superlinear increase in the vortex inductance.

It is interesting to verify whether the measured slope $L_v/B_z = 118$ nH/mT is compatible with Eq. 1 of the main text, with a reasonable assumption for k. From the theory we know that $k \approx 0.25dB_c^2/\mu_0$ [5, 6], where $B_c = 13.9$ mT is the thermodynamic critical field and $d \simeq 4.5$ nm [7] the effective Al thickness, i.e. the nominal one minus 2.5 nm of oxide. With this value of k, using Eq. 1 we obtain $L_v/B_z = N_\square\Phi_0/k = 36$ nH/mT, which is of the same order of magnitude as the measured value. The factor three discrepancy between the expected and the measured value of L_v/B_z is acceptable, in particular when considering the relatively large theoretical uncertainty for the numerical prefactor 0.25 [5]. Also, our synthetic Rashba superconductor has a complex structure along the z direction (a metallic film, an insulating barrier and a proximitized 2DEG), which is clearly not considered in the simple models.
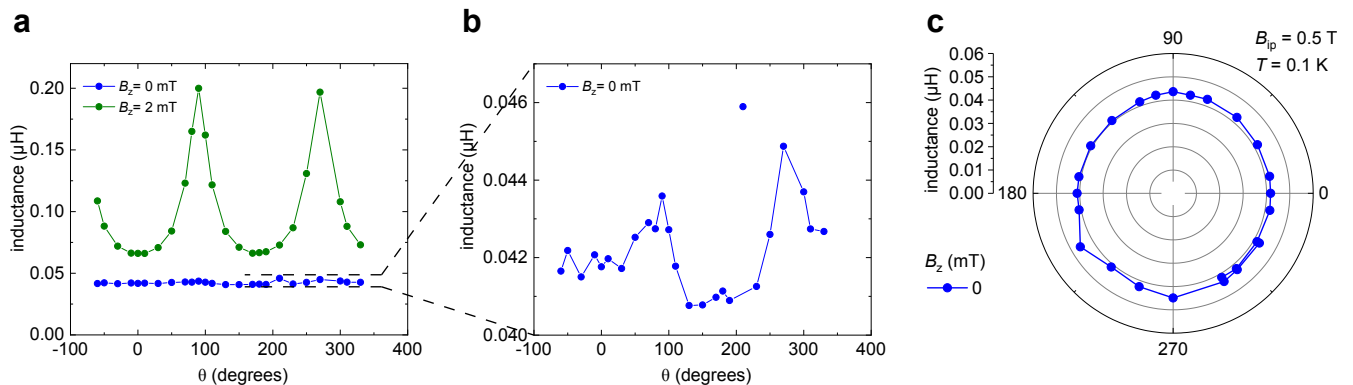
FIG. S1. **a,** Inductance measured for $B_z = 0$ mT (blue) and $B_z = 2$ mT (green) as a function of the angle θ between in-plane field $\vec{B}_{ip}$ and current $\vec{I}$, for $|\vec{B}_{ip}| = 0.5$ T and $T = 0.1$ K. The graph corresponds to that in Fig. 2**b** of the main text, displayed in a cartesian plot. **b,** Zoom in order to highlight the data for $B_z = 0$. The outlier is most probably caused by a flux jump in the compensation coil. **c,** Same data as in panel **b**, but displayed in a polar plot.

ISOTROPY OF THE KINETIC INDUCTANCE IN THE ABSENCE OF VORTICES

Figure S1 focuses on the inductance measurements at $B_{ip} = 0.5$ T for $B_z = 0$ mT (blue) and $B_z = 2$ mT (green). The former case corresponds, in good approximation, to the absence of vortices, while the latter case to a small but finite vortex density. In this section we show how different is the symmetry of the inductance measured in the two cases.

Panel **c** shows a magnified view of the inductance curve for the $B_z = 0$ case in Fig. 2**b** of the main text. This nearly isotropic graph must be compared to the highly anisotropic ones at finite B_z in Fig. 2**b**. For ease of comparison we displayed both the graph for $B_z = 0$ (blue) and for $B_z = 2$ mT (green) in a cartesian plot, see Fig. S1**a**. The residual anisotropy, barely discernible in the zoom-in plot displayed in panel **b**, might be due to residual vortices. In fact, the orthogonal coils used for compensating B_z (the compensation procedure is outlined in the last section) produce a field which is not *perfectly* homogeneous. As a consequence, if the sample is large, it is possible to locally have uncompensated vortices, even when the average B_z is globally set to zero. Since vortices provide a much larger inductance contribution than the bare kinetic inductance, their effect can be important. Therefore, Fig. S1 sets an *upper limit* for the anisotropy of the bare kinetic inductance, which is evidently very low.

From Fig. S1 we deduce that, at least in good approximation, the superfluid density is isotropic even when subjected to in-plane fields. In the absence of Lifshitz invariant terms in the free energy, one would then expect a similar isotropy also for the vortex core structure (and correspondingly for the measured vortex inductance). The observed strong anisotropy of L_v for finite B_z and B_{ip} is a strong signature of the Lifshitz invariant. This is further corroborated by control measurements in samples with largely reduced SOI (see next section), where both pinning enhancement and inductance anisotropy are *not* observed.

ISOTROPY OF KINETIC INDUCTANCE AND VORTEX INDUCTANCE IN Al/GaAs SAMPLES

Figure S2 shows the results of inductance measurements performed on our control sample. As mentioned in the main text, this sample is a meander structure similar to the main device discussed in this work, see Fig. 1**b** of the main text. This meander is patterned starting from a heterostructure consisting of Al grown on top of a GaAs substrate. While the Al film is similar to that grown on InAs, the absence of a quantum well, together with the reduced atomic weight of Ga compared to In, guarantees that SOI is greatly reduced.

The graph in Fig. S2 shows the inductance measured on such control device for selected values of B_{ip}, B_z and θ. For $B_{ip} < 1$ T the inductance is nicely isotropic. Also, as anticipated in the main text (Fig. 2**a**, grey symbols) the vortex inductance increases with B_{ip}. Only at very large B_{ip} *and* at finite B_z, a slight anisotropy emerges. Such anisotropy is comparable with the data point scatter and it is much smaller than the vortex anisotropy observed in the epitaxial Al/InAs sample discussed in the main text. Data in Fig. S2 unambiguously demonstrate the crucial role of the SOI in determining the observed anisotropic vortex squeezing.
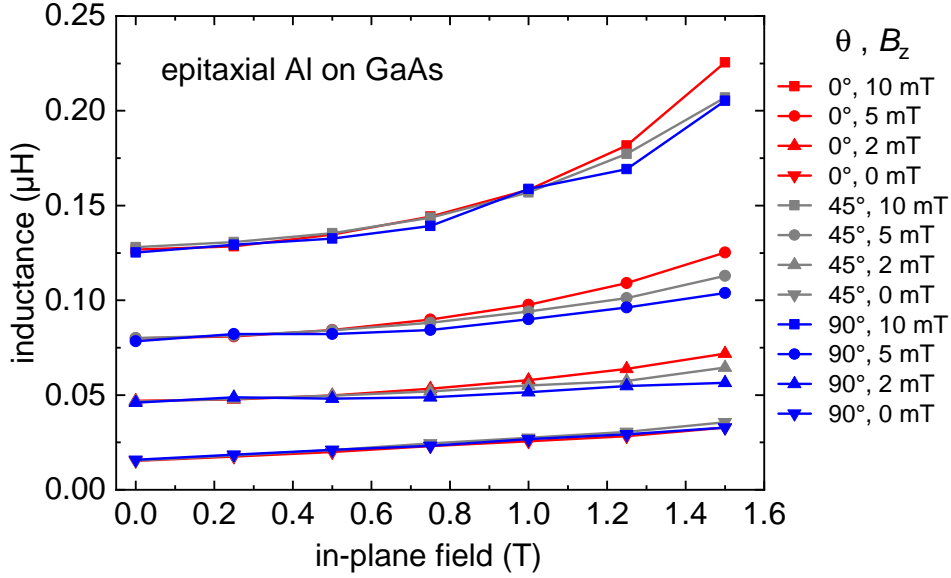

FIG. S2. Inductance measured on a meander device patterned on a Al/GaAs sample, where spin-orbit effects are largely reduced. Measurements are performed for different angles θ between in-plane field $\vec{B}_{ip}$ and current $\vec{I}$ [$\theta = 0°$ (red), $\theta = 45°$ (grey), $\theta = 90°$ (blue)], for different values of B_z [0 mT ($\triangledown$), 2 mT ($\triangle$), 5 mT ($\square$), 10 mT ($\bigcirc$)] and of B_{ip} [abscissas]. We notice that the inductance always monotonically increases. The anisotropy in the inductance is negligible: it can only be discerned for finite B_z (vortex inductance) and large B_{ip} (larger than 1 T).

WEAK ANISOTROPY FOR $B_{c,ip}$

Figure S3 shows the temperature dependence of the in-plane critical magnetic field $B_{c,ip}$. The critical field values correspond to the emergence of a resistance $R(B_{c,ip}) = 0.5R_n$ where the normal state resistance $R_n = 9.2$ Ω. The measurement has been repeated for $\theta = 0°$ (blue curve, $\mathbf{B}_{ip}$ parallel to the current) and for $\theta = 90°$ (red curve, $\mathbf{B}_{ip}$ perpendicular to the current).

We notice a small anisotropy (of the order of 8%) in $B_{c,ip}$, which implies the same anisotropy for $\xi \propto B_{c,ip}$. Since the width and thus the curvature of the potential $U(\mathbf{r})$ scale as ξ, in principle the anisotropy in ξ should determine an anisotropy in the measured vortex inductance. From a quantitative point of view, however, the observed ξ anisotropy is too small to justify a large difference between $L_v(\theta = 0°)$ and $L_v(\theta = 90°)$. In fact, the ratio $L_v(\theta = 0°)/L_v(\theta = 90°)$ (i.e. the ratio $k_\perp/k_\parallel$) is about 4.7 at $B_{ip} = 1$ T, see Fig. 2**c** of the main text.

What we learn from the small anisotropy in the in-plane critical field $B_{c,ip}$ (Fig. S3) and in the kinetic inductance L_s (Fig. S1) is that the presence of $\mathbf{B}_{ip}$ does impact the isotropy of the condensate (as highlighted by recent studies [4]), but this effect is small and thus insufficient to explain the strong anisotropy of the vortex inductance. On the other
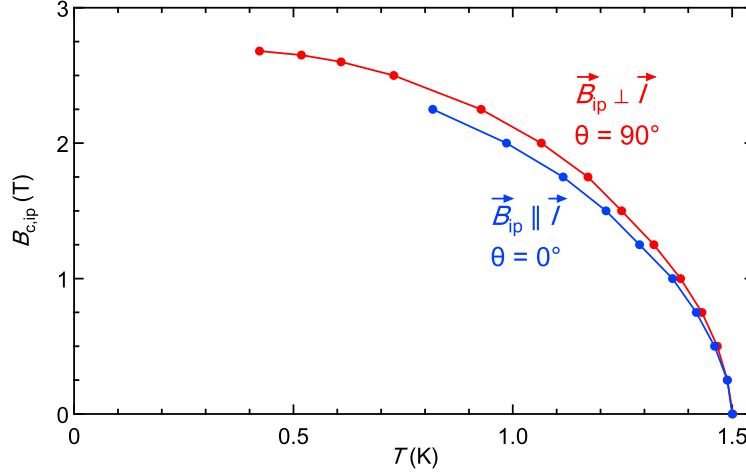
FIG. S3. The graph shows the critical in-plane magnetic field $B_{c,ip}$ as a function of the temperature T for $\theta = 90°$ (red, $\mathbf{B}_{ip} \perp \mathbf{I}$) and $\theta = 0°$ (blue, $\mathbf{B}_{ip} \parallel \mathbf{I}$).

hand, the vortex anisotropy naturally emerges as a result of the Lifshitz invariant term in the Ginzburg-Landau free energy.

VORTEX INDUCTANCE FOR LOW IN-PLANE FIELDS: ZOOMING IN FIG. 2a

Figure S4 shows a zoom-in view of the low in-plane field region in Fig. 2a of the main text. The graph makes it evident that what in the full range graph in Fig. 2a appeared as noise near zero field, is indeed a double peak with a cusp-like minimum at zero, where the values for $\theta = 90°$ and $\theta = 0°$ become approximately equal. This double-peak is visible also for the $\theta = 0°$ data (blue in Fig. S4), although in a less pronounced fashion.

The study of these peaks is beyond the scope of this article. Investigation on these peaks is ongoing, and it will be discussed elsewhere.
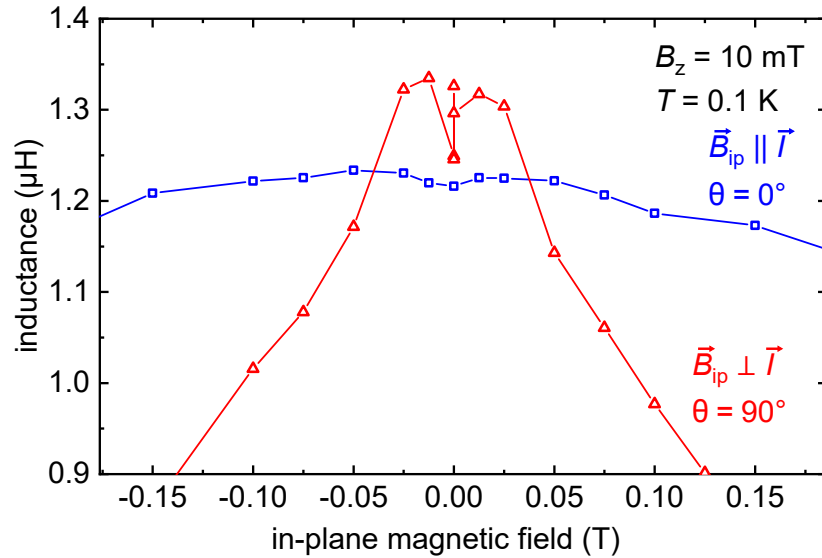

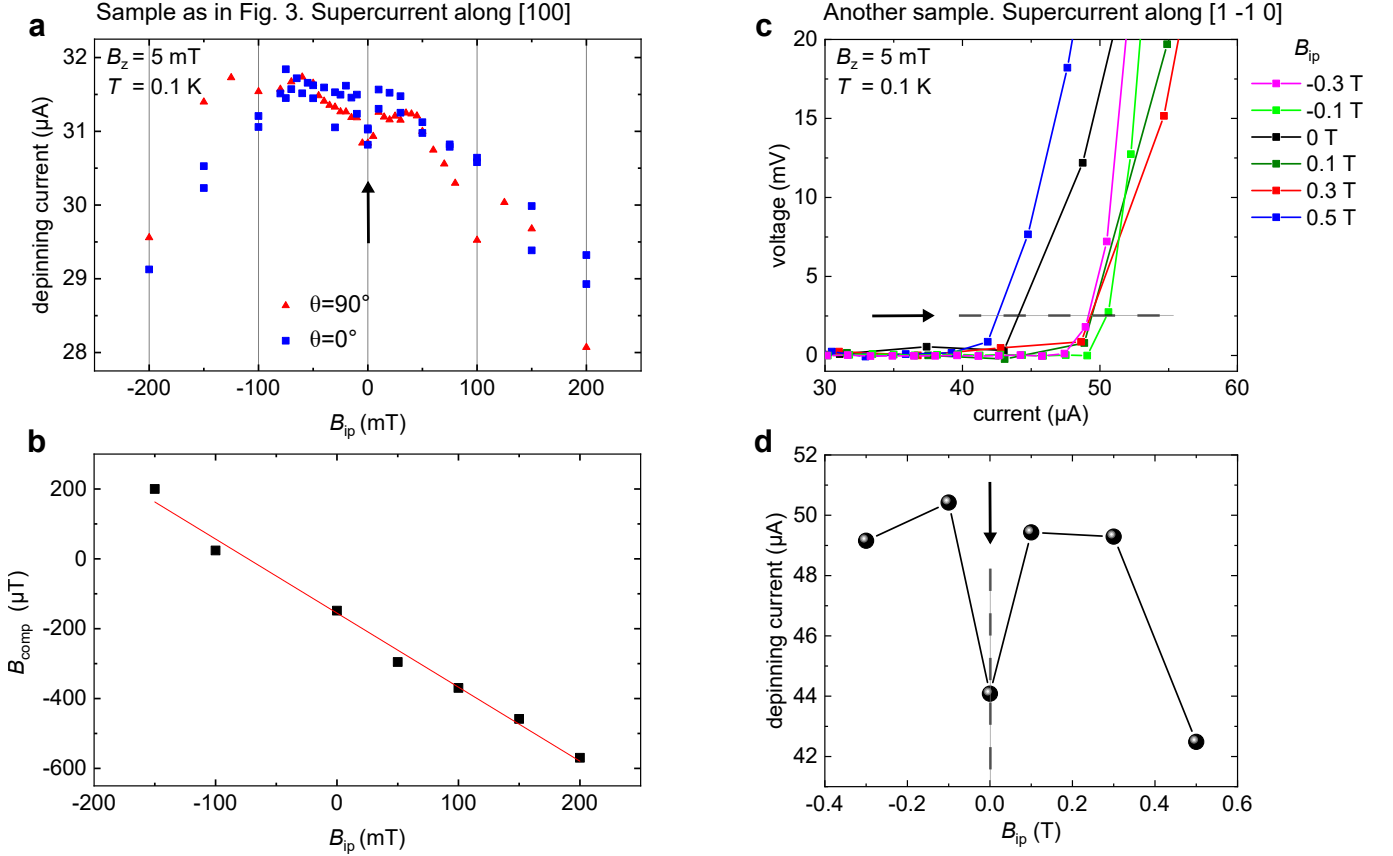FIG. S4. Zoom-in of Fig. 2a of the main text.

FIG. S5. **a,** Depinning current versus in-plane field B_{ip}, measured at $B_z = 5$ mT for in-plane field perpendicular (red symbols $\theta = 90°$) and parallel (blue symbols $\theta = 0°$) to the current. The measurement is performed on the same sample discussed in Fig. 3 of the main text, where the current is directed along the [100] crystallographic direction. The arrow indicates the anomalous minimum at zero field. **b,** Out-of-plane field $B_{comp}(B_{ip})$ that must be applied to obtain an effective zero out-of-plane field B_z in the measurements in panel **a**. The finite slope originates from the misalignment of $\mathbf{B}_{ip}$, which is not perfectly perpendicular to B_z. **c,** IV-characteristics measured on a different device, with the same geometry as the one of the previous panels, but oriented along the [1-10] crystallographic direction. The arrow indicates the threshold (2.5 µV) used to determine the depinning current. **d,** Depinning current as a function of the in-plane field for the latter sample. A minimum at zero field is again visible, indicated by the arrow.

FURTHER MEASUREMENTS OF THE DEPINNING CURRENT VERSUS IN-PLANE FIELD

In this section we shall discuss further measurements of the in-plane field dependence of the depinning current. These measurements were performed with different orientations of the in-plane magnetic field with respect to the current ($\theta = 0°$ and $\theta = 90°$). At the end of the section, we also present measurements on a different device.

Figure S5a shows the same measurements reported in Fig. 3 of the main text (red symbols, $\theta = 90°$), together with the same measurements performed with the in-plane field oriented parallel to the current (blue symbols, $\theta = 0°$). We notice that the minimum of the depinning current at zero bias (black arrow) is reproducible. The minimum for $\theta = 0°$ is less pronounced compared to that for $\theta = 90°$, which possibly mirrors the fact that the anomalous inductance decrease is less pronounced for $\theta = 0°$ compared to $\theta = 90°$, see Fig. 2 of the main text.

We stress that the depinning current measurements here shown were much more difficult compared to inductance measurements, owing to the fact that the devices we used had a very large contact resistance. These required the use of very fast (9 ms) IV sweeps, followed by long cooling times (30 s). More importantly, the large resistance made it impossible to make use of the compensation field routine described in the next section, which we followed for the inductance measurements. In this case we followed a different routine, described in the following:

1. The desired in-plane field B_{ip} is set.

2. The B_z field component is set to the expected zero value.

3. The sample is heated above T_c, then a waiting time of 15 minutes allows the sample to cool down to base temperature.

4. A series of of IV-traces is taken for different B_z values. The set $B_z = B_{comp}$ value such that critical current is maximal is taken as effective $B_z = 0$ value.

5. The operations above are repeated for several in-plane field values B_{ip} that cover the desired range of values for the final measurements. As a result, one obtains a graph as the one in Fig. S5**b**, showing the necessary $B_{comp}(B_{ip})$ component necessary to compensate the each B_{ip}.

After $B_{comp}(B_{ip})$ is determined, we start the final measurement of the depinning current versus B_{ip}, by applying for each B_{ip} the corresponding compensation field plus 5 mT, i.e., $B_z^{comp}(B_{ip}) + 5$ mT. Then, the sample is heated above T_c, cooled down back to base temperature, then finally 45 IVs are measured as discussed in the main text. As an alternative, we applied the compensation routine at each B_{ip} point. This is the case of the $\theta = 0°$ points (blue symbols) in Fig. S5**a**. However, this makes the entire measurement series much longer, with an increased risk of drift of important measurement parameters.

In Fig. S5**c,d** we show depinning current measurements versus in-plane field for another device, with exactly the same geometry as the one discussed above. In this case, however, the current (i.e., the axis of the Hall bar) is directed along the [1-10] crystallographic direction. Again, each depinning current value is determined after averaging of many fast IV-characteristics. The orientation of the in-plane field is $\theta = 90°$, while the out-of-plane $B_z = 5$ mT. The panel **c** shows selected IV characteristics, while panel **d** shows the deduced depinning current values as a function of B_y. Again, we observe a clear minimum at zero-field, consistent with our other observations reported above and with the inductance measurements in the main text. As for the anomalous inductance decrease discussed in the Fig. 2 of the main text, this anomalous increase of the pinning strength is a clear signature of the impact of the Lifshitz invariant on the condensate.

OUT-OF-PLANE FIELD COMPENSATION PROCEDURE

Owing to misalignment of the different parts of the cryostat, the sample surface will hardly be *perfectly* parallel to the axis of the main superconducting coil, which we use to apply the in-plane field $\mathbf{B}_{ip}$. Owing to the large inductive contribution of vortices, the undesired out-of-plane component of $\mathbf{B}_{ip}$ will have a significant impact on the inductance measurements. In particular, it will mask the measurement of the kinetic inductance of the condensate. For measurements that demand zero out-of-plane magnetic field, residual out-of-plane field components must be manually compensated using additional orthogonal coils. In this section we outline the procedure we used to zero the out-of-plane field in inductance measurements. The ideas is to identify a physical quantity which is very sensitive to the absolute perpendicular fields, as e.g. the resistance near the superconducting transition near the critical temperature. In Fig. S6 a typical compensation measurement is depicted. In this case, the resistance of the sample slightly above the critical temperature (see inset of Fig. S6) is measured. In this regime, the resistance is strongly dependent on the perpendicular field, which is applied via the additional orthogonal coils. Perpendicular field sweeps are always performed back and forth to ensure that the resistive response is non-hysteretic in order to exclude e.g. flux trapping. The compensation field is determined by finding the minimum of a parabolic fit of the magnetoresistance data measured in the fluctuation regime of the superconductor. In that regime surface barriers for vortex entry and exit are absent and hence magnetoresistance curves are non-hysteretic. With this procedure the compensation field can be easily determined with an uncertainty below 10 μT.

The perpendicular field B_{comp} needed to compensate for the sample misalignment is therefore

$$B_{comp}(B_{ip}) = B_{ip} \sin(\alpha), \tag{S.64}$$

where α is the angle between the film plane and the applied in-plane field $\mathbf{B}_{ip}$. The compensation field is clearly proportional to B_{ip}. Owing to the imperfect homogeneity of the compensation field, together with the fact that the sample position within the field distribution changes with θ (since the rotation axis of the piezo is not perfectly centered on the sample), the misalignment angle α also depends on θ. Thre angle α is typically less than 2°.
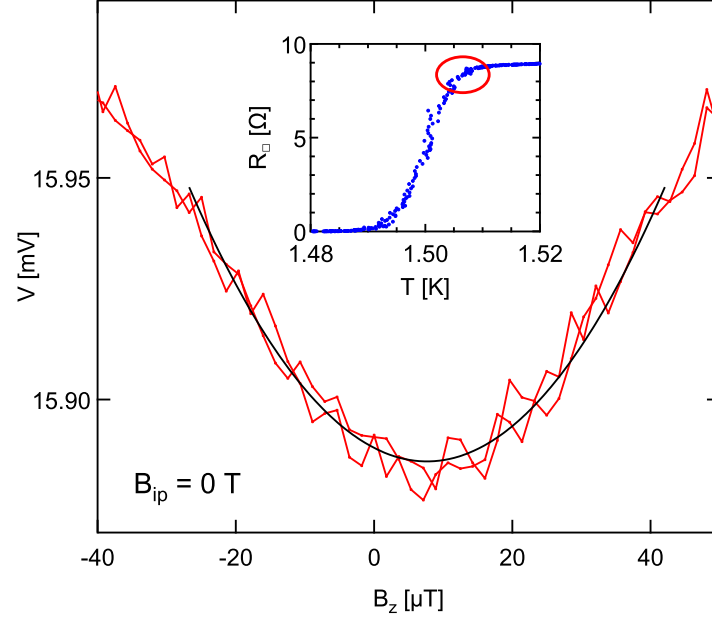
14

FIG. S6. Exemplary magnetoresistance measured at $T > T_c$. Data are taken at a temperature corresponding to the fluctuation regime of the superconductor, where $R(B_z)$ is non-hysteretic. This regime is highlighted in the inset. Black solid line is a parabolic fit to the measured data.

* nicola.paradiso@physik.uni-regensburg.de

[1] V. M. Edelstein, The Ginzburg - Landau equation for superconductors of polar symmetry, Journal of Physics: Condensed Matter **8**, 339 (1996).

[2] M. Tinkham, *Introduction to Superconductivity: Second Edition (Dover Books on Physics) (Vol i)*, 2nd ed. (Dover Publications, 2004).

[3] At low field, temperature and bias, when the sample inductance is negligible compared to the external inductance of the RLC circuit, the resistance which is sufficient to damp the resonance is just about $1\ \Omega$. However, when the field is increased and approaches the critical value, the sample inductance diverges. Since the Q factor scales as $(\sqrt{L/C})/R$, the increase in sample inductance compensate the effect of the damping resistance. Therefore, near the critical field the resistance at which the resonator becomes overdamped is $65\ \Omega$, which is much larger than $1\ \Omega$, but still much less than the normal resistance.

[4] D. Phan, J. Senior, A. Ghazaryan, M. Hatefipour, W. M. Strickland, J. Shabani, M. Serbyn, and A. P. Higginbotham, Detecting induced $p \pm ip$ pairing at the Al-InAs interface with a quantum microwave circuit (2021), arXiv:2107.03695 [cond-mat.supr-con].

[5] M. Golosovsky, M. Tsindlekht, and D. Davidov, Radio-Frequency Resistance in the Mixed State for Subcritical Currents, Supercond. Sci. Technol. **9**, 1 (1996).

[6] G. Blatter, M. V. Feigel'man, V. B. Geshkenbein, A. I. Larkin, and V. M. Vinokur, Vortices in high-temperature superconductors, Rev. Mod. Phys. **66**, 1125 (1994).

[7] T. Wang, C. Thomas, R. E. Diaz, S. Gronin, D. Passarello, G. C. Gardner, M. A. Capano, and M. J. Manfra, The dependence of aluminum lattice orientation on semiconductor lattice parameter in planar InAs/Al hybrid heterostructures, Journal of Crystal Growth **535**, 125570 (2020).